Multiscale porosity estimates along the pro- and retrograde deformation path: an example from Alpine slates

Ismay Vénice Akker[1], Josef Kaufmann[2], Guillaume Desbois[3], Jop Klaver[4], Janos L. Urai[3], Alfons Berger[1], Marco Herwegh[1]

5   [1]Institute of Geological Sciences, University of Bern, Bern, CH-3012, Switzerland
[2]Empa, Swiss Federal Laboratories for Materials Testing and Research, Dübendorf, CH-8600, Switzerland
[3]Structural Geology, Tectonics and Geomechanics, Energy and Mineral Resources Group, RWTH Aachen University, Aachen, 52056, Germany
[4]Structural Geology, Tectonics and Geomechanics, Energy and Mineral Resources Group, RWTH Aachen
10 University, Aachen, 52056, Germany & Map Microstructures and Pores GmbH, Aachen, 52056, Germany

Correspondence to: Ismay Vénice Akker (ismay.akker@geo.unibe.ch)

Abstract. Estimating porosity of slates is of great interest for the recently rising industries dealing with the
15 underground such as CO_2 sequestration, nuclear waste disposal and shale gas but also for engineering purposes in terms of mechanical stability for underground or surface constructions. In this study, we aim understanding estimates of porosity of slates from the Infrahelvetic Flysch Units (IFU) in the Glarus Alps (eastern Switzerland) and their changes as function of varying metamorphic grade. Surface and sub-surface samples are collected along a temperature gradient from 200 to 320 °C and give therefore the opportunity to link pore types along the
20 deformation path and to surface processes or indicate what artificially induced porosity is. A developed workflow consists of a combination of bulk rock measurements such as Helium pycnometry (He-pycnometry) and Mercury Intrusion Porosimetry (MIP) with image analysis. Image analysis is performed on high scale resolution with Scanning Electron Microscopy (SEM) on Broad Ion Beam (BIB) prepared cross sections (BIB-SEM). Different vein generations give evidence for porosity formation at depth. Towards peak metamorphic conditions (prograde
25 path) porosity reduces to <1 vol%, indicated by matrix porosity detected by BIB-SEM, as this technique has shown the least artificially induced porosity by polishing. During exhumation (retrograde path) porosity increases due to the formation of microfractures interpreted as the effect of unloading (open fractures). At the surface, porosity is further increased due to the formation of macrofractures (up to 1 mm), which are interpreted to be the effect of weathering processes such as freeze and thaw cycles or these are artificially induced by sample preparation.
30 Additionally, porosity and pore morphology are strongly dependent on mineralogy, sample homogeneity and strain.

1. Introduction

Slates as representatives of sheet-silicate-rich rocks delineate a fine-grained anisotropic microstructure and are common low-grade metamorphic rocks. These rock types play an important role in the rising industry of
35 underground storage, such as nuclear waste disposal and geological carbon sequestration (e.g. Loon, 2008; Thury and Bossart, 1999) but are also of importance in surface and subsurface building industry because of the low mechanical strength and associated geotechnical problems. Moreover, slates are crucial during mountain building processes, since they can act as a mechanically weak phase as they localise large amounts of strain in low- and

very low-grade metamorphic domains (e.g. Labaume et al., 1997; Milliken and Reed, 2010; Warr et al., 2014). Secondly, slates act as important fluid sources, liberating water with progressive compaction and metamorphic reaction (e.g. Dielforder et al., 2015; Rieke and Chilingarian, 1974). The pore network defines the major fluid pathways and detailed investigation of microstructural porosity would be a key to better understand the fluid flux and circulation of fluids in collisional orogens and orogenic wedges.

The porosity of a rock develops along the deformation path and with changing PT conditions. A possible evolution starts with early compaction and diagenesis on the prograde path evolving to maximum burial, followed by metamorphism and possibly tectonic deformation on the retrograde path eventually resulting in surface exposure (Horseman et al., 1996). The first aim of this study is to give an estimate of the total present-day porosity of a slate, which underwent this full deformation-metamorphic cycle. The second goal is to find the meaning of this present-day total porosity in terms of which processes along the evolution path account for what type of porosity. For this study, we focus on surface collected slates from the Infrahelvetic Flysch Units (IFU) in the Glarus Alps (eastern Switzerland), which are affected by large out-of-sequence thrusts, such as the Glarus thrust (e.g. Badertscher et al., 2002; Burkhard et al., 1992; Ebert et al., 2007; Herwegh et al., 2008; Pfiffner et al., 2011; Poulet et al., 2014; Rahn and Grasemann, 1999; von Daeniken and Frehner, 2017). This specific area is of interest because it covers a temperature gradient, which positively correlates with a background strain gradient, directly related to the metamorphic conditions. With tectonic processes changing along this gradient from soft sediment behaviour including particulate flow, at the lowest temperatures, to pressure solution at higher temperatures (Dielforder et al., 2016). Investigating porosity over this gradient would give insight in the evolution of porosity at geological conditions.

A variety of methods have been developed over the past decades to determine porosity, pore morphology and pore size distribution, each having a characteristic pore size range (Anovitz and Cole, 2015). Some common direct approaches include gas expansion techniques such as helium pycnometry (He-pycnometry) and Mercury Intrusion Porosimetry (MIP) (Anovitz and Cole, 2015; Tiab and Donaldson, 2015). These techniques both yield information on the bulk interconnected porosity in 3D volumes. Recent developments of surface preparation based ion beam milling (Focused Ion Beam (FIB) and Broad Ion Beam (BIB)) allow imaging porosity down to nanometer scale on an almost perfectly flat surface with a Scanning Electron Microscope (SEM). These images are suitable for high quality image segmentation.

Porosity estimates obtained with bulk rock measurements yield information of large sample volumes but remain unresolved in terms of contribution of different pore morphologies. Therefore, most studies use a combination of bulk rock measurements with image analysis (using He-pycnometry: e.g. Houben et al., 2016: Yang et al., 2016 and MIP: e.g. Hemes et al., 2013; Klaver et al., 2012, 2015 and MIP, SIP, NMR, μ-CT: Zhang et al., 2018). Most of this research is focused on shales or clay(stones). In this study, we aim to apply such a workflow to slates. In contrast to shales, slates show an enhanced coehsion, higher rock strength and define a stronger anisotropic microstructure due to increased metamorphism, deformation and dehydration. Particularly because of the latter, the contribution of (micro)fractures plays an important role as fluid pathways in these slate samples. We aim to find out if such fractures result only from surface processes or are already formed at depth. In addition, there is a strong contrast between samples collected from subsurface drillcores and surface outcrops in terms of the effect of unloading due to stress changes during exhumation and finally it is necessary to distinguish original porosity from artificially induced porosity.

2. Samples and geological background

Slates are selected from the IFU in the Glarus Alps in eastern Switzerland (Fig. 1a). The flysch units are deposited in the underfilled Northern Alpine Foreland Basin and accreted in-sequence to the accretionary wedge during subduction of the European margin (Lihou, 1996). The IFU consists of the North Helvetic flysch (NHF), which is

5   overthrusted by the South Helvetic flysch and Ultrahelvetic flysch, the latter including the Sardona and Blattengrat unit. The names of the flysch units refer directly to the paleographic realm in which they were deposited (Lihou, 1996). The Ultrahelvetic flysch is itself overthrusted by the Subhelvetic units and the Helvetic nappes along the Glarus thrust (Pfiffner, 1986; Schmid, 1975; Trümpy, 1969). In this thrust wedge the overburden of the flysch relates to 8-12 km corresponding to lower greenschist metamorphic conditions (Frey et al., 1980; Lihou, 1996;

10   Rahn et al., 1995).

The flysch units include heterogeneous end-members from volcano-clastic turbiditic sandstones and dark slates (Fig. 1b; Siegenthaler, 1974). These rocks show indications, such as folding of bedding parallel calcite veins, of soft sediment deformation behaviour (Dielforder et al., 2016). Late Cretaceous limestones and marls are indicative for the Sardona and Blattengrat unit, which occur towards the south of the study area (Fig. 1c) (Bisig, 1957;

15   Leupold, 1942; Lihou 1995; Trümpy, 1969).

The compositions of the slates from the flysch units are heterogeneous comprising layered mineralogical variations owing to turbiditic sedimentation processes. In this study, we focus on the clay-(mica)-rich layers excluding sandy layers from our analysis. We collected eight samples from the flysch between the village "Weesen" in the north and the locality "Flims" in the south (Fig. 1a). All samples are from surface outcrops, except for samples D and E,

20   which are from the abandoned sub-surface slate mine (=Landesplattenberg). The N-S sample profile across the Flysch units covers a change in peak metamorphic conditions from 200 °C in the north to 320 °C in the south determined by calcite/dolomite thermometry and Raman spectroscopy of carbonaceous material (Ebert et al., 2007; Lahfid et al., 2010). This gradient correlates to a strain gradient, as the most southern units were subducted to the deepest levels prior to in-sequence imbricate stacking.

3. Analytical techniques

3.1 Bulk rock porosity

3.1.1 Helium pycnometry (=He-pycnometry)

He-pycnometry is performed on oven dried (115 °C) plugs with a 2.5 cm diameter and geometrical volumes >5

30   cm^3 (Fig. 2). Plugs are drilled in the hand samples (Fig. 3a) and after drilling the flat surfaces of the plugs are polished to obtain the best cylindrical shape. The geometrical volume is defined by an average of 6 calliper measurements of the height and 4 measurements of the diameter of the plug. Pycnometric density measurements are obtained from an AccuPyc 1330 pycnometer. Performance of the machine is related to sample quantity and cell size. The accuracy of the porosity measurements of the machine falls between 0.02 vol% and 0.1 vol% (Viana

35   et al., 2002). Helium is used as specific gas as its small radius of the atoms are assumed to percolate the sample volume until the smallest pore sizes (1 nm). Drilling of plugs resulted in some cases in splitting of the rock along the foliation planes, resulting in several thin cylindrical plugs (Fig. 3b-c). To increase the sample quantity and reduce the analytical error, these samples (<10 % of the sample chamber) are analysed simultaneously. When the

plug volume exceeded 10 vol% of the sample volume chamber, an average of two adjacent plugs is taken. The amount of purges was set to ten and the connected porosity is calculated by Eq. (1).

$$\text{connected porosity} = 1 - \frac{\text{bulk density}}{\text{grain density}}$$

For He-pycnometry, the sample volume has shown to effect the measurements, with larger sample volumes resulting in lower porosity (Table S1). Duplo measurements yield absolute differences of about 0.03–0.07 vol%. The difference between measuring different layers, several cylinders simultaneously, compared to an average of separate layers yields a maximum difference of about 0.5 %. Therefore, the error, used as the standard deviation

10   of the different measurements, is set to 0.5 vol%.

3.1.2 Mercury Intrusion Porosimetry (=MIP)

MIP is applied on oven dried (115 °C) sample volumes of clay(mica)-rich layers taken from the close vicinity of the plugs used for He-pycnometry measurements. Sample material is cut in wet conditions, using water, by means of a diamond saw so that the measured pieces have a 4–5 mm edge length. In one measurement, three to five pieces

15   are analysed.

The analyses are performed using Thermoelectron Pascal 140/440 equipment. In a first step, mercury was intruded to a maximum pressure of 200 kPa. Then the sample was moved to the Pascal 440 machine for high-pressure analysis up to 200 MPa. Pore sizes are calculated using Washburn's equation (Washburn, 1921). For the analyses, a cylindric pore shape with a contact angle of 140° and a surface tension of mercury of 0.48 N/m porosimetry was

20   assumed leading to intruding a minimal pore radius of 3.7 nm.

MIP is performed in a multi cycle experiment, including two full injection and extrusion cycles. Assumed is that ink-bottle type pores remain filled after first intrusion and that in a second intrusion the pores are successively filled with mercury (e.g. big pores followed by smaller pores). The first cycle indicates the complete pore volume, the second cycle only the connected pores, which include the small pore fraction (Fig. 4). Subtraction of the second

25   cycle from the first cycle gives the size of the neck pore entrances at which the 'ink-bottle type pores' become filled (Kaufmann, 2010; Kaufmann et al., 2009). All errors of this technique fall into the 5 vol% range.

3.2 High resolution imaging techniques

At first, a regular petrographic light microscope is used to examine the petrography and microstructure of the samples. In addition, a Virtual Petrography (ViP) dataset is created from a subset of thin sections at the GED

30   institute-RWTH Aachen. Such a dataset is created using an automated petrographic microscope, which under various polarisation and illumination conditions (parallel polarized and crossed polarized) digitises complete thin sections at high resolution (e.g. 45.000 x 30.000 pixel maps for a thin section of 3x2 cm (Virgo et al., 2016). The scanned thin sections can be viewed with Petroscan TileViewer and allows changing the polarization angle digitally from the interpolated layers. Such an environment works as a 'digital microscope' in which it is possible

35   to directly select microstructural domains of interest. For this study, we selected only areas from clay (mica)-rich intervals and excluded large-scale fractures (Fig. 3d-e).

3.2.1 BIB sample preparation

To examine the effect of mechanical polishing of thin sections in terms of induced artificial porosity, surface low-angle ion polishing is performed on 2D surfaces of thin sections (circular areas of about 2.6 cm diagonally). Ion polishing is performed with a Leica EM TIC 3X argon ion stand-alone polisher (6 kV, 2 mA, 3 °, 8 h) at the

5   Institute of Geological Sciences (University of Bern).

Additionally, slope cut ion polishing is performed on the sample material. These samples are cut from clay (mica)-rich layers with a diamond saw under wet conditions and have dimensions of about 5x7x3 mm. Cross sections are made in the 7x3 mm side and are about 1–2 mm^2 in size. Slope cutting is performed with a JEOL SM-09010 BIB argon cross-section polisher (6 kV, 90 °, 8 h). The BIB cross sections are coated with tungsten.

10   SEM imaging using different sample preparation is shown in Figure 5. The mechanically polished thin section shows many polishing damage effects such as breakouts of pores. These effects are not seen in both ion polished samples (ion polished 2D thin section and BIB-SEM). The advantage of the ion polished 2D thin section method is that it obtains larger areas of high quality, but striations on the surface remain. The BIB-SEM obtains smaller areas, but of very high quality that allow microstructural imaging down to nm-scale (e.g. Hemes et al., 2015). Both

15   ion polish techniques yield better results than mechanical polishing because there is: (1) no smearing of clay, (2) no breakage of mineral grains and (3) no polishing dust filling pores.

3.2.2 Microstructure imaging

A Zeiss EVO 50 SEM with backscatter and secondary electron detectors at the Institute of Geological Sciences (University of Bern) is used to obtain images from the mechanical polished thin sections. Image mosaics (0.4–0.6

20   mm^2) are acquired using a magnification of 400x consisting of ten to fifteen images. Images from BIB prepared samples are taken with a Zeiss Supra 55 SEM with backscatter and secondary electron detectors (GED, RWTH Aachen). Both overview image mosaics with a magnification of 125x and 1250x and high magnification (up to 20 kx) are acquired. For testing the Representative Element Area (REA) the box counting method is used (Kameda et al., 2006; Klaver et al., 2012). Hereby, we applied a stepwise growing box to the segmented pore images in

25   which the total area% of pores within the box is measured. At a certain box size the total area% does not significantly vary anymore, this box size is taken as the REA. We checked this for two different samples using BIB-SEM images (Fig. 6). Sample A shows a minimum REA of about 900 µm^2, whereas sample C requires a minimum REA of at least 25000 µm^2. The microstructure reveals the differences between those REA's. In the following, image analysis are presented on areas between 1750 and 31500 µm^2.

30   ### 3.2.3 Image analysis

Images were first cleaned by manually removing of artefacts, such as dust or charging effects. Images are segmented using manually thresholding in ImageJ version 1.51n (Schindelin et al., 2012; Schneider et al., 2012). This software is also used for the pore analysis. The outlines of the analysed particles are projected as overlay on the original images in Photoshop CS 5.1 to optimize the thresholding values. Pores are classified by their

35   morphology, based on the ratio minor axis over major axis (b/a). If this ratio is <0.2 the pore is considered as fracture. This criterion comes from the b/a vs. area % plot shown in Figure S1. This plot shows that for values b/a <0.3 the porosity steeply increases as the effect of fractures. We choose a value for fractures b/a <0.2 to make sure that everything below this value is indeed a fracture. Manual pore segmentation yields a human error of about 10

averaged and the standard deviation was taken as mean error. The highest given standard deviation is than applied
to all samples, assuming all samples behave identically. The standard deviation of the porosity obtained by image
analysis from mechanical polished thin sections is 0.5 area% and for BIB-SEM prepared samples 0.15 area%.

4. Results

4.1. Microstructure, petrography and sample heterogeneity

The slates are defined by alternating intervals of silty and clay (mica)-rich layers (mm - cm scale) owing to
turbiditic sedimentation processes. The clay (mica)-rich layers include four dominant mineral phases: mica,
chlorite, quartz and calcite and in minor components: dolomite, albite, pyrite and rutile. Mica occurs in two distinct
phases: 1) relatively large mica aggregates up to 20–50 µm in size, often deformed. These aggregates occur both
aligned and randomly oriented with respect towards the foliation plane, 2) relatively small mica grains (1-5 µm)
mostly aligned in the foliation plane.

The alignment of the sheet-silicates in the foliation plane forms the main fabric. The low temperature end-member
(sample A: $T_{max}=$ 200 °C, Fig. 7a,b) delineates no preferred alignment of minerals. This is a low strain end-
member as inferred by the occurrence of undeformed fossils in a clay-rich matrix. Sample E ($T_{max}=$ 250 °C, Fig.
7c,d) shows the alignment of mica and an increase of microfractures along the grain boundaries of mica. The high
temperature end-member (Sample H: $T_{max}=$ 320 °C Fig. 7e,f) delineates a strong and defined spaced cleavage
with pressure solution seams and shows no fossils. This sample also represents the high strain end-member,
indicated by the elongation of detrital quartz and calcite crystals. An overview of microstructures of all the samples
is given in Figure S2.

Vertical and horizontal sample heterogeneity is reflected in the approach shown in Figure 3. We analyzed two
adjacent drill cores (core axis is bedding perpendicular), which were measured as sub-layers along the foliation
planes. He-pycnometry results show that the porosity bedding perpendicular shows substantial variations between
1.4 and 5.2 vol% (sample plug G1: Fig. 3b). Only small variations <0.8 vol% are seen bedding parallel, meaning
that within the sample volume the sub-layers of each plug correlate laterally very well and are therefore relatively
homogeneous. Despite the bedding perpendicular porosity variation, accompanied image analysis of the same
sample material demonstrates a homogenous lithological composition (Fig. 3c). The porosity variation across these
layers is primarily due to the local occurrence of fractures.

4.2 Pore morphology

Porosity consists of two main groups classified by pore morphology: 1) macrofracture porosity, which includes
macrofractures with apertures up to several mm and length of few mm to cm. Such large-scale fractures are
immediately visible in thin sections and greatly influence bulk rock measurements. 2) The matrix porosity consists
of matrix pores, including inter- and intraparticle pores and microfractures (apertures between 1–5 µm). Matrix
porosity is measured by image analysis on areas selected in between such identified macrofractures.

Image analysis on mechanical polished thin sections have shown porosity estimates from these thin sections are
unreliable. The only reliable information those analyses give is insight in the contribution of microfractures. In
contrast, BIB-SEM prepared samples yield flat 2D surfaces and give a good insight in the complete matrix porosity.

4.2.1 Macrofracture porosity

Macrofractures can be subdivided in: (1) open fractures, in most cases these fractures are bedding parallel and occur on the foliation planes as seen in the preparation plugs and by UV light detection of the fracture network of a sub-sample (Fig. 3e). In thin sections such fractures are recognized by the relatively large size in both aperture

5 (>10 µm) and length, as these run through the complete section. Sometimes material is smeared into the fractures during mechanical polishing (Fig. 8a-b). They show no precipitation of secondary minerals after fracturing (2) open veins, these contain mineral precipitates, but remain a high porosity and (3) completely mineralized veins.

4.2.2 Matrix porosity

Image analysis on BIB-SEM prepared samples allows discriminating the matrix porosity in two types of pores: (1)

10 microfractures, defined by an aspect ratio of b/a <0.2, have apertures of about 1−5 µm and are not continuous (length up to 30 µm). In Figure 8, a special type of fracture porosity is seen in fine-grained mica-rich layers, which accommodate brittle strain. Inside the fractures also pyrite precipitated, demonstrating a geological origin of these fractures. In such samples, the fracture porosity is the largest contribution to the total porosity. These fractures are often located along the grain boundaries of micas and in some cases along quartz (Figs. 8 and 9d and 10a). The

15 second pore type comprises (2) non-fracture-related pores, mostly interlayer pores associated with mica and clay minerals or due to dissolution along grain boundaries of quartz (Fig. 9c-d). Intraparticle pores occur in minor quantity in calcite, dolomite (Fig. 9c-d and 10b) or quartz (Fig. 10e-f). Such pores are often related to quartz and calcite cement, which occurs in some cases as new infill of fossils (Fig. 10c) or fluid inclusions.

4.3 Quantification of porosity

20 All porosity estimates obtained by the different techniques applied in this study are given in Table 1 and Figure 11. Note that the techniques each have an own characteristic resolution (Fig. 2a). Moreover, He-pycnometry and MIP both obtain a connected porosity. Image analysis yields microfractures, inter- and intraparticle pores. Microfractures and interparticle pores have the greatest contribution to the total porosity in our sample set as seen by microstructural imaging (Fig. 8 and 9).

25 Porosity of the bulk rock of the slates, obtained by He-pycnometry, show that the samples have a connected porosity in the range between 0.7–7.2 vol% (Fig. 11). Moreover, He-pycnometry results show a bulk density of 2.55–2.73 g/cm^3 and grain density of 2.73–2.78 g/cm^3.

The MIP results show variations in porosity from 0.4–2.7 vol%, not in all samples directly correlating with the He-pycnometry data. Pore volumes with a pore throat radius and fracture apertures between 5 and 20 nm have the

30 largest contribution to the total porosity (Fig. 12a and b). In addition, a slightly increased frequency of pores with a radius and fracture apertures between 100 and 200 nm is seen. In Figure 13 the neck pore entrances, which is the interpolated difference between the 1st and the 2nd intrusion cycle is plotted vs. the cumulative pore volume. The samples C, G and H have the highest bulk porosity (Fig. 13). The second cycle contains much less remaining mercury in the pores, as the intrusion and extrusion curve approach each other (Fig. S3). The correction, which is

35 applied, comes from the assumption that for extrusion another contact angle applies (110°; Kaufmann, 2010). Hence, the correction is only for extrusion data. The hysteresis between the second intrusion and extrusion almost disappears by applying the above explained pore size correction. This is more evident for sample C than for sample H, which indicates a slight increase in hysteresis.

Image analysis from thin sections show fracture porosities between 0.04–1.8 area%. Image analysis from BIB-SEM reveals total (fracture plus matrix) porosity estimates between 0.3–1.4 area%, much lower compared to the above presented bulk approaches. Pore size distributions from image analysis (BIB-SEM) show a similar trend as the MIP data (Fig. 12) for pore sizes >30 nm. Where there is a peak in the 100–200 nm pore radius in the BIB-

5   SEM data, there is also an elevation in the MIP data, although not with the same contribution. In addition, the MIP data indicate a major pore radius ~10 nm, which cannot be measured by image analysis because of resolution limits.

Figure 11 shows an exponential decrease with asymptotic behaviour for decreasing sample input from bulk rock measurements to image analysis. There exists no direct trend along the temperature and indirect strain gradient

10   from sample A to H for any of the measurement techniques (see varying color-coded symbols in Figure 11 between the different approaches). Nonetheless, knowing the microstructure enables to interpret the outcome of the porosity results. Sample C, with relatively high amount of large mica grains yields the highest porosity values (for all techniques). The highest-grade samples G and H, also show relative high porosity for MIP, due to bedding parallel microfractures. Whereas, sample A, which is the weakly deformed homogenous clay sample plots at the lower end

15   of the diagram, indicating lower porosity (for MIP and BIB-SEM). The sub-surface samples (sample D and E), which are from the close vicinity of sample C, show in general a lower porosity given in He-pycnometry and MIP than given for the mechanically polished thin section of sample C.

5. Discussion

In this work, we use a workflow, which includes validating bulk rock measurements with high-resolution imaging

20   using BIB-SEM to differentiate porosity data of slates. In a second step, we link these estimates for the present-day porosity to processes along the PTt-deformation path.

5.1 Contribution to porosity estimates

Artificially induced porosity is often due to sample collection and preparation. During sample collection, artefacts

25   like fracturing could rise from hammering, transport or storage (drying). Sample preparation, like cutting, and mechanical polishing of thin sections could induce significant additional artificial porosity, such as breakouts, resulting in apparent porosity values without geological meaning (Fig. 5). Therefore, for image analysis procedures on slate samples, sample preparation like ion polishing techniques, either on 2D thin sections or on cross sections of sub-samples are necessary (e.g. Hemes et al., 2013; Houben et al., 2013, Keller et al., 2013; Klaver et al., 2012,

30   2015).

The bulk rock measurements are strongly influenced by the presence of natural and possible artificial fractures and sample heterogeneity. This results in non-correlating He-pycnometry and MIP data. Differences in porosity estimates from bulk rock measurements and image analysis techniques are related to the different principles underlying the techniques, which namely are the sample volumes (Ougier-Simonin et al., 2016) and the limits in

35   spatial resolution (e.g. Hemes et al., 2013). In addition, Kaufhold et al. (2016) acknowledge the resolution issue by a comparison of MIP with FIB-SEM data from shales and shows that only 20 vol% of the total porosity can be resolved with FIB-SEM, the remaining porosity content should be measured with a bulk rock measurement technique such as He-pycnometry. Additionally, large microfractures are not incorporated in the representative domain of the BIB-SEM, but do play an important role in the MIP data (Hemes et al., 2013). This correlates to our

observations: larger cracks are measured in the bulk rock methods, whereas the BIB-SEM data only provide matrix porosity as we avoid imaging the large fractures. Hence, using a combination of such methods, the REA of the image analysis does not necessarily need to cover the full range of pore sizes. However, the BIB-SEM investigation links the bulk He-pycnometry and MIP to each other. MIP measures the macrofractures and matrix porosity (>3.7

5   nm eq. pore throat radius) while the He-pycnometry measures the total porosity (>1 nm eq. pore throat radius) without providing information on the pore type while the BIB-SEM does.

Porosity types from different scales seem to be related with each other (Fig. 11). A sample with many small-scaled microfractures has also the highest amount of macrofractures, seen by a relative high contribution in bulk rock porosity. Although, BIB-SEM yields sections of pore bodies in 2D images and MIP pore volume (3D). There is a

10   correlation of pore size distributions between those two datasets in the overlapping measured scale (Fig. 12). For the overlapping size range of these two methods, these methods are comparable to each other (see also Houben et al., 2013), indicating 2D data are sufficient to estimate average values. Each measurement technique has its characteristic pore size range that can properly be analysed, which means that combining different methods results in overlapping scales, allowing to resolve the porosity from nm to cm scale.

15   Our analysis shows that sample inhomogeneity between the internal slate layers can be large. It comprises original sedimentary variations, such as clay (mica)-rich layers alternated by silt-rich layers. For bulk rock measurements the REV is dependent on the clay content and grain size distribution of sand grains for the different sediment layers (e.g. carbonates and quartz): the higher the clay content relative to the non-clay content, the smaller the REV (Keller, 2015).

20   In light of a comparison of our slate results with previous studies performed on clay stones as precursor rocks of slates, MIP ranges reported for the poorly compacted "Boom clay" (local name of Jurassic clay in France) are about 35–40% (Boisson, 2005). Boom clay has a high pore connectivity and it is shown that in samples with a higher clay content the pore connectivity is controlled by pores in the clay matrix, whereas in samples with a smaller clay content large interparticle pores have the largest contribution to the total connectivity (e.g. Hemes et

25   al., 2013). A second clay stone type, the "Opalinus clay" (local name of Jurassic clay in Switzerland), is more compacted and cemented than the Boom clay (about 10% porosity from MIP: Houben and Urai, 2013 and references therein). It shows smaller values for connected porosity and like in the Boom clay, the clay matrix controls the permeability. In contrast to these clay stones, the slates from our study show 0.4–2.7 vol% porosity from MIP measurements and the pores in the clay matrix are not visible on the scale of the SEM. This means the

30   sheet-silicate matrix is much tighter in these slates, which experiences higher PT-conditions and show in contrast to the Boom clay and Opalinus clay pressure solutions seams, elongated grains and a much smaller number of fossils due to recrystallization, diagenesis, dissolution and precipitation mechanisms. In these higher-grade samples, the clay minerals are replaced by micas and due to their strong anisotropy (micro)fractures, as also illustrated by the BIB-SEM images of sample H, are the main factor contributing to pore connectivity. As a result,

35   the porosity and pore morphology from slates in this study are not directly comparable to the pore types reported for diagenetic clays (e.g. Boom clay; Opalinus clay) but show an advanced stage of porosity reduction owing to increased metamorphic overprint.

5.2 Processes influencing porosity

To understand what part of the total connected porosity obtained with the bulk rock measurements is fracture porosity and what part is matrix porosity, image analysis can be used as a threshold. Figure 11 shows that image analysis gives an estimate of the matrix porosity. Subtracting the BIB-SEM matrix porosity from the MIP bulk

5 rock measurements yields the macrofracture porosity. Subtracting the MIP porosity from the He-pycnometry gives insight in the smallest matrix pores.

Dielforder et al. (2016) estimated for convergent plate boundaries that porosity decreases from 60 to 10 % within the upper 5 km of the accretionary wedge along the prograde metamorphic gradient applying theoretical considerations (see references in Dielforder et al., 2016). Along this prograde evolution, the tectonic processes

10 change from soft sediment deformation like particulate flow to pressure solution (Dielforder et al., 2015, 2016). The porosity evolution found in this study is shown in Figure 14 and shows different vein generations on both the prograde and retrograde evolution. Veins are indicative for brittle failure and can therefore be used as indicators for ancient fracture porosity at the stage prior to fracture sealing by precipitation of the vein minerals. The earliest formed fracture porosity is shown by deformed shear-veins overprinted by the main foliation (stage I). From initial

15 sedimentation to maximum burial the rock texture changes from an undeformed matrix with randomly oriented sheet-silicates to a slate with a well-developed spaced cleavage and strong structural anisotropy (Fig. 7). The porosity decreases from 60 vol% (Dielforder et al., 2016) to values <0.9 vol% at maximum burial (peak metamorphism). This is reflected by the matrix porosity obtained by image analysis on BIB-SEM prepared sub-samples from the underground mine of Landesplattenberg. At these highest reached temperatures, dynamic

20 recrystallization of bedding parallel veins takes place (Fig. 14: stage II). On the prograde path, the sediments are strongly influenced by compaction together with dehydration and diagenesis as shown by diagenetic quartz and/or calcite cement precipitation. Diagenetic cementation processes play an important role as porosity reducing mechanism in these slates accompanying dissolution by pressure solution (e.g. Katsube and Williamson, 1994). Generally, pressure solution also decreases porosity but there exist also pore forming processes by dissolution such

25 as pores in and around dolomite (Fig. 10b). This newly created porosity, however, is of minor importance and is far beyond the amount of pore destruction by pressure solution.

Along the temperature and correlated strain gradient from Weesen (200 °C) to Flims (320 °C), there seems to be no relation between porosity and temperature/strain neither in the bulk rock measurements nor in the images analysis results. However, local variations in mineralogy and strain influence the porosity: a high sheet-silicate

30 content leads to a strong anisotropic fabric, resulting in an increase of microfractures and therefore in a higher porosity (sample C). An only weakly deformed sample, with a less defined fabric, results in a low porosity (sample A). This means that porosity and pore morphology are closely related to the mineralogical composition, spatial heterogeneity of the phase distributions and strain (e.g. Janssen et al., 2011; Keller et al., 2013). Together with aforementioned temporal porosity changes by fracturing and vein mineral precipitation, the prograde local porosity

35 evolution can therefore be rather variable and dynamic in time but yields in a general decrease of the average porosity with increasing burial.

The porosity on the retrograde path is mainly characterized by fracturing and the formation of bedding parallel, sometimes partly recrystallized veins, veins oblique to the bedding and abundant microfractures (Fig. 14: resp. stages III, IV and V). In a first stage, these microfractures evolve in an isolated, but spatially dispersed manner

40 along clay-rich layers. Sometimes pyrite and/or calcite precipitated in such microfractures clearly pointing to a

fracturing at still metamorphic conditions (Fig. 8). According porosity values are represented by the fracture porosity obtained from bulk rock measurements of sub-surface samples (Fig. 14). Such microfractures are likely the effect of unloading. Dielforder et al. (2016) link the pressure solution processes and the illite-muscovite transformation to an embrittlement during the prograde path. Such embrittlement allows the dominance of

5   microfractures (e.g. Zeng et al., 2013), which could be an additional factor causing the formation of such microfractures. Along the retrograde path this effect is enhanced, because temperatures are decreasing again, allowing the further increase of size and amount of fractures. With progressive exhumation the microfractures grow and eventually interconnect transferring microfractures to fractures (Fig. 14). The increasing porosity can also be resealed by deformation and disaggregation. The formation of clay gouge could reduce the created porosity

10   such that a cataclastically deformed slate becomes a clay (Holland et al., 2006).

In the light of near surface porosity formation, plotting fracture porosity from bulk rock measurements of surface collected samples and comparing them with the underground sample reveals the contribution on porosity formation by surface processes such as fracturing. In the surface collected samples, which are exposed to strongly varying

15   climatic conditions, such fractures could be due to freeze and thaw cycles (Cárdenes et al., 2012) but also to unloading during deglaciation resulting in exfoliation jointing (Jahns, 1943; Ziegler et al., 2016). Particularly in the case of the mechanically highly anisotropic slates, the pre-existing foliations are prone for reactivation of these structural planes by fracturing during the youngest climate- and weathering-related processes. Additionally, macrofractures can in many cases also be artificially induced, requiring discrimination between artificial and

20   young geological fracturing processes. Principally, we can list two discrimination criteria. Near surface fractures experience infiltration of meteoric water resulting in oxidation of Fe-bearing mineral phases such as iron sulfides (e.g. pyrite). Consequently thin layers of iron hydroxides form appearing as faint reddish staining along the fracture planes. Hence, this staining provides clear evidence for an in situ crack formation in the rock within its natural environment. In contrast, preparation-induced fractures will not show such staining phenomena. Moreover, these

25   fractures mostly contain small amounts of polishing material, which is smeared during this mechanical treatment into the newly created fracture (Fig. 8). This accumulation is not possible in the case of priory resin-impregnated natural fractures. Despite these two unequivocal criteria, it might be difficult to discriminate between the two late fracture types in cases where none of the two evidences is present.

6. Conclusion

30   In this study, we use a combination of He-pycnometry and MIP as bulk rock measurements and image analysis to obtain estimates of porosity of slates. Bulk rock measurements obtain the total connected porosity, which can be subdivided in fracture and matrix porosity determined by image analysis. Image analysis from BIB-SEM images yield information about the matrix porosity including intra- and interparticle pores and microfractures. This matrix porosity reflects the porosity at maximum burial (peak metamorphism) and is strongly influenced by diagenetic

35   processes on the prograde path. Subtracting the matrix porosity from the total porosity obtained by bulk rock measurements yield the fracture porosity and matrix porosity below BIB-SEM resolution. Most of the microfractures are bedding parallel or occur along the grain boundaries of mica and are subscribed to the effect of unloading on the retrograde path. Macrofractures (up to 1 mm) are in many cases related to surface processes such as freeze and thaw cycles or are artificially induced by sample preparation. Different vein generations show that

the formation of porosity is not restricted to unloading or surface processes but fracturing took place along the entire *PT*t-deformation path. In a temporal point of view, the porosity variability must be rather dynamic, given the stages of pore opening owing to fracturing and subsequent sealing by mineral precipitation. Moreover, porosity and pore morphology are strongly dependent on mineralogy, homogeneity and strain. The multiscale approach

5   coming from shales, which links microporosity to macroporosity by combining bulk rock measurements with image analysis, is in this study successfully applied to slates.

7. Acknowledgements

For this project funding is received from the Swiss National Science Foundation (SNSF; grant number 162340). We thank Simon Virgo from RWTH Aachen University for creating the ViP dataset and Thomas Aebi and Stephan

10   Brechbühl from the University of Bern for their help with sample preparations.

References

Anovitz, L. M., and Cole, D. R.: Characterization and analysis of porosity and pore structures, Rev. Mineral. Geochem., 80, 61-164, 2015.

Badertscher, N. P., Beaudoin, G., Therrien, R., and Burkhard, M.: Glarus overthrust: A major pathway for the escape of fluids out of the Alpine orogen, Geology, v. 30, no. 10, p. 875-878, 2002.

Bisig, W.K.: Blattengratflysch und Sardonaflysch im Sernftal nördlich der Linie Richetlipass – Elm – Ramintal – Grosse Scheibe, PhD Thesis Nr. 2435, ETH Zürich, Switzerland, 239 pp, 1957.

Boisson, J.Y.: Clay Club Catalogue of Characteristics of Argillaceous Rocks, OECD/NEA/RWMC/IGSC (Working Group on measurement and Physical understanding of Groundwater flow through argillaceous media) august 2005 Report NEA no. 4436 (Brochure and CD-Rom including data base), OECD/NEA, Paris, France, p. 72, 2005.

Burkhard, M., Kerrich, R., Maas, R., and Fyfe, W.: Stable and Sr-isotope evidence for fluid advection during thrusting of the Glarus nappe (Swiss Alps), Contrib. Mineral. Petr., v. 112, no. 2, p. 293-311, 1992.

Cárdenes, V., Monterroso, C., Rubio, A., Mateos, F., and Calleja, L.: Effect of freeze–thaw cycles on the bending strength of roofing slate tiles, Eng. Geol., 129, 91-97, 2012.

Dielforder, A., Vollstaedt, H., Vennemann, T., Berger, A., and Herwegh, M.: Linking megathrust earthquakes to brittle deformation in a fossil accretionary complex, Nat. Commun., 6, 2015.

Dielforder, A., Berger, A., and Herwegh, M.: The accretion of foreland basin sediments during early stages of continental collision in the European Alps and similarities to accretionary wedge tectonics, Tectonics, 2016.

Ebert, A., Herwegh, M., and Pfiffner, A.: Cooling induced strain localization in carbonate mylonites within a large-scale shear zone (Glarus thrust, Switzerland), J. Struct. Geol., 29, 1164-1184, 2007.

Frey, M., Teichmüller, M., Teichmüller, R., Mullis, J., Künzi, B., Breitschmid, A., Gruner, U., and Schwizer, B.: Very low-grade metamorphism in external parts of the Central Alps: illite crystallinity, coal rank and fluid inclusion data, Eclogae Geol. Helv., v. 73, no. 1, p. 173-203, 1980.

Hemes, S., Desbois, G., Urai, J., De Craen, M., and Honty, M.: Variations in the morphology of porosity in the Boom Clay Formation: insights from 2D high resolution BIB-SEM imaging and Mercury injection Porosimetry, Neth. J. Geosci., 92, 275-300, 2013.

Hemes, S., Desbois, G., Urai, J. L., Schröppel, B., and Schwarz, J.-O.: Multi-scale characterization of porosity in Boom Clay (HADES-level, Mol, Belgium) using a combination of X-ray µ-CT, 2D BIB-SEM and FIB-SEM tomography, Micropor. Mesopor. Mat., 208, 1-20, 2015.

Herwegh, M., Hürzeler, J. P., Pfiffner, O. A., Schmid, S. M., Abart, R., & Ebert, A.: The Glarus thrust: excursion guide and report of a field trip of the swiss tectonic studies Group, Swiss Geological society, 14.–16. 09. 2006, Swiss J. Geosci., *101*(2), 323-340, 2008.

Holland, M., Urai, J. L., van der Zee, W., Stanjek, H., and Konstanty, J.: Fault gouge evolution in highly overconsolidated claystones, J. Struct. Geol., v. 28, no. 2, p. 323-332, 2006.

Horseman, S., Higgo, J., Alexander, J., and Harrington, J.: Water, gas and solute movement through argillaceous media, Nuclear Energy Agency Rep. CC-96/1. OECD, Paris, 1996.

Houben, M. E., and Urai, J.: In situ characterization of the microstructure and porosity of Opalinus Clay (Mont Terri Rock Laboratory, Switzerland), PhD thesis, Von der Fakultät für Georessourcen und Materialtechnik Der Rheinisch-Westfälischen Technischen Hochschule Aachen, 2013.

Houben, M., Desbois, G., and Urai, J.: Pore morphology and distribution in the Shaly facies of Opalinus Clay (Mont Terri, Switzerland): Insights from representative 2D BIB–SEM investigations on mm to nm scale, Appl. Clay Sci., 71, 82-97, 2013.

Houben, M., Barnhoorn, A., Lie-A-Fat, J., Ravestein, T., Peach, C., and Drury, M.: Microstructural characteristics
5   of the Whitby Mudstone formation (UK), Mar. Petrol. Geol., 70, 185-200, 2016.

Jahns, R. H.: Sheet structure in granites: its origin and use as a measure of glacial erosion in New England, J. Geol., 51, 71-98, 1943.

Janssen, C., Wirth, R., Reinicke, A., Rybacki, E., Naumann, R., Wenk, H.-R., and Dresen, G.: Nanoscale porosity in SAFOD core samples (San Andreas Fault), Earth Planet Sc. Lett., 301, 179-189, 2011.

10   Kameda, A., Dvorkin, J., Keehm, Y., Nur, A., Bosl, W.: Permeability–porosity trans-forms from small sandstone fragments, Geophysics 71, N11–N19, 2006.

Katsube, T., and Williamson, M.: Effects of diagenesis on shale nano-pore structure and implications for sealing capacity, Clay Miner., 29, 451-472, 1994.

Kaufhold, S., Grathoff, G., Halisch, M., Plötze, M., Kus, J., Ufer, K., Dohrmann, R., Ladage, S., and Ostertag-
15   Henning, C.: Comparison of methods for the determination of the pore system of a potential German gas shale, in: Filling the Gaps: from Microscopic Pore Structures to Transport Properties in Shales, The Clay Minerals Society, 163-190, 2016.

Kaufmann, J.: Pore space analysis of cement-based materials by combined Nitrogen sorption–Wood's metal impregnation and multi-cycle mercury intrusion, Cement Concrete Comp., 32, 514-522, 2010.

20   Kaufmann, J., Loser, R., and Leemann, A.: Analysis of cement-bonded materials by multi-cycle mercury intrusion and nitrogen sorption, J. Colloid Interf. Sci., 336, 730-737, 2009.

Keller, L. M.: On the representative elementary volumes of clay rocks at the mesoscale: Journal of Geology and Mining Research, 7, 58-64, 2015.

Keller, L. M., Holzer, L., Schuetz, P., and Gasser, P.: Pore space relevant for gas permeability in Opalinus clay:
25   Statistical analysis of homogeneity, percolation, and representative volume element, J. Geophys. Res-Sol. Ea., 118, 2799-2812, 2013.

Klaver, J., Desbois, G., Urai, J. L., and Littke, R.: BIB-SEM study of the pore space morphology in early mature Posidonia Shale from the Hils area, Germany, Int. J. Coal Geol., 103, 12-25, 2012.

Klaver, J., Hemes, S., Houben, M., Desbois, G., Radi, Z., and Urai, J.: The connectivity of pore space in mudstones:
30   insights from high-pressure Wood's metal injection, BIB-SEM imaging, and mercury intrusion porosimetry, Geofluids, 15, 577-591, 2015.

Labaume, P., Maltman, A., Bolton, A., Tessier, D., Ogawa, Y., and Takizawa, S.: Scaly fabrics in sheared clays from the décollement zone of the Barbados accretionary prism, PROCEEDINGS-OCEAN DRILLING PROGRAM SCIENTIFIC RESULTS, 59-78, 1997.

35   Lahfid, A., Beyssac, O., Deville, E., Negro, F., Chopin, C., and Goffé, B.: Evolution of the Raman spectrum of carbonaceous material in low-grade metasediments of the Glarus Alps (Switzerland), Terra Nova, 22, 354-360, 2010.

Leupold, W.: Neue Beobachtungen zur Gliederung der Flyschbildungen der Alpen zwischen Reuss und Rhein, Eclogae Geol. Helv., 35(2), 247–291, 1942.

Loon, V. L.: Preferred orientations and anisotropy in shales: Callovo-Oxfordian shale (France) and Opalinus Clay (Switzerland), Clay Clay Miner., 56, 285-306, 2008.

Lihou, J.: A new look at the Blattengrat unit of eastern Switzerland: Early Tertiary foreland basin sediments from the South Helvetic realm, Eclogae Geol. Helv., 88(1), 91–114, 1995.

5   Lihou, J.: Structure and deformational history of the Infrahelvetic flysch units, Glarus Alps, eastern Switzerland, Eclogae Geol. Helv., 89(1), 439, 1996.

Milliken, K., and Reed, R.: Multiple causes of diagenetic fabric anisotropy in weakly consolidated mud, Nankai accretionary prism, IODP Expedition, 316, 1887-1898, 2010.

Ougier-Simonin, A., Renard, F., Boehm, C., and Vidal-Gilbert, S.: Microfracturing and microporosity in shales, Earth-Sci. Rev., 162, 198-226, 2016.

10   Pfiffner, A.O.: Evolution of the north Alpine foreland basin in the Central Alps. In: Foreland Basins, Int. Assoc. Sediment. Spec. Publ., Volume 9, 219–228, 1986.

Pfiffner, O. A., Ramsay, J., and Schmid, S.: Structural map of the Helvetic Zone of the Swiss Alps: Geological special map, v. 1, no. 100,000, 2011.

15   Poulet, T., Veveakis, M., Herwegh, M., Buckingham, T., and Regenauer-Lieb, K.: Modeling episodic fluid-release events in the ductile carbonates of the Glarus thrust, Geophys. Res. Lett., v. 41, no. 20, p. 7121-7128, 2014.

Rahn, M., and Grasemann, B.: Fission track and numerical thermal modeling of differential exhumation of the Glarus thrust plane (Switzerland), Earth Planet Sc. Lett., v. 169, no. 3-4, p. 245-259, 1999.

Rahn, M., Mullis, J., Erdelbrock, K., and Frey, M.: Alpine metamorphism in the north Helvetic flysch of the
20   Glarus-Alps, Switzerland, Eclogae Geol. Helv., v. 88, no. 1, p. 157-178, 1995.

Rieke, H. H., and Chilingarian, G. V.: Compaction of argillaceous sediments, Elsevier, 1974.

Schindelin, J., Arganda-Carreras, I., Frise, E., Kaynig, V., Longair, M., Pietzsch, T., Preibisch, S., Rueden, C., Saalfeld, S., and Schmid, B.: Fiji: an open-source platform for biological-image analysis, Nat. Methods, v. 9, no. 7, p. 676, 2012.

25   Schmid, S.M.: The Glarus overthrust: field evidence and mechanical model, Eclogae Geol. Helv., 68(2), 247–280, 1975.

Schneider, C. A., Rasband, W. S., and Eliceiri, K. W.: NIH Image to ImageJ: 25 years of image Analysis, Nat. Methods, v. 9, no. 7, p. 671, 2012.

Siegenthaler, C.: Die nordhelvetische Flysch-Gruppe im Sernftal (Kt. Glarus), Unpublished PhD Thesis,
30   University of Zurich, 83 pp, 1974.

Thury, M., and Bossart, P.: The Mont Terri rock laboratory, a new international research project in a Mesozoic shale formation, in Switzerland, Eng. Geol., 52, 347-359, 1999.

Tiab, D., and Donaldson, E. C.: Petrophysics: theory and practice of measuring reservoir rock and fluid transport properties, Gulf professional publishing, 2015.

35   Trümpy, R.: Die Helvetischen Decken der Ostschweiz; Versuch einer palinspastischen Korrelation und Ansätze zu einer kinematischen Analyse, Eclogae Geol. Helv., 62(1), 105–142, 1969.

Viana, M., Jouannin, P., Pontier, C., and Chulia, D.: About pycnometric density measurements, Talanta, 57, 583-593, 2002.

Virgo, S., Heup, T., Urai, J. L., and Berlage, T.: Virtual Petrography (ViP)-A virtual microscope for the
40   geosciences, EGU General Assembly Conference Abstracts, Vienna, 17-22 April 2016, 14669, 2016.

von Däniken, P. A., and Frehner, M.: 3D structural model and kinematic interpretation of the Panixer Pass Transverse Zone (Infrahelvetic Complex, eastern Switzerland), Swiss J. Geosci., v. 110, no. 2, p. 653-675, 2017.

Warr, L. N., Wojatschke, J., Carpenter, B. M., Marone, C., Schleicher, A. M., and van der Pluijm, B. A.: A "slice-and-view" (FIB–SEM) study of clay gouge from the SAFOD creeping section of the San Andreas Fault at∼ 2.7

5   km depth, J. Struct. Geol., 69, 234-244, 2014.

Washburn, E. W.: The dynamics of capillary flow, Phys. Rev., 17, 273, 1921.

Yang, R., He, S., Yi, J., and Hu, Q.: Nano-scale pore structure and fractal dimension of organic-rich Wufeng-Longmaxi shale from Jiaoshiba area, Sichuan Basin: Investigations using FE-SEM, gas adsorption and helium pycnometry, Mar. Petrol. Geol., 70, 27-45, 2016.

10   Zeng, W., Zhang, J., Ding, W., Zhao, S., Zhang, Y., Liu, Z., and Jiu, K.: Fracture development in Paleozoic shale of Chongqing area (South China). Part one: Fracture characteristics and comparative analysis of main controlling factors, J. Asian Earth Sci., 75, 251-266, 2013.

Zhang, Z., Kruschwitz, S., Weller, A., and Halisch, M.: Enhanced pore space analysis by use of μ CT, MIP, NMR, and SIP, Solid Earth Discuss., v. 2018, p. 1-23, 2018.

15   Ziegler, M., Loew, S., and Amann, F.: Near-surface rock stress orientations in alpine topography derived from exfoliation fracture surface markings and 3D numerical modelling, Int. J. Rock Mech. Min., 85, 129-151, 2016.

| sample | latitude | longitude | Bulk rock porosity | | Image analysis | | | |
			He-pycnometry [vol%]	MIP [vol%]	SEM thin section fracture porosity [area%]	BIB-SEM total porosity [area%]	fracture porosity [area%]	matrix porosity [area%]
A	47°08'26.3" N	9°06'26.1" E	-	0.51	0.04	0.26	0.13	0.13
B	46°59'47.2" N	9°05'20.9" E	3.3	-	0.46	-	-	-
C	46°59'13.9" N	9°09'17.6" E	7.2	2.67	1.84	1.39	0.49	0.90
D	46°58'12.0" N	9°09'19.7" E	0.7	0.66	-	-	-	-
E	46°58'12.0" N	9°09'19.7" E	2.6	1.27	-	-	-	-
F	46°57'34.3" N	9°11'23.6" E	1.6	0.39	0.21	-	-	-
G	46°53'17.2" N	9°07'40.1" E	4.2	2.58	0.05	-	-	-
H	46°53'29.0" N	9°11'22.4" E	2.3	2.28	0.51	0.35	0.20	0.15

Table 1. Samples, coordinates and porosity estimates from each different measurement technique
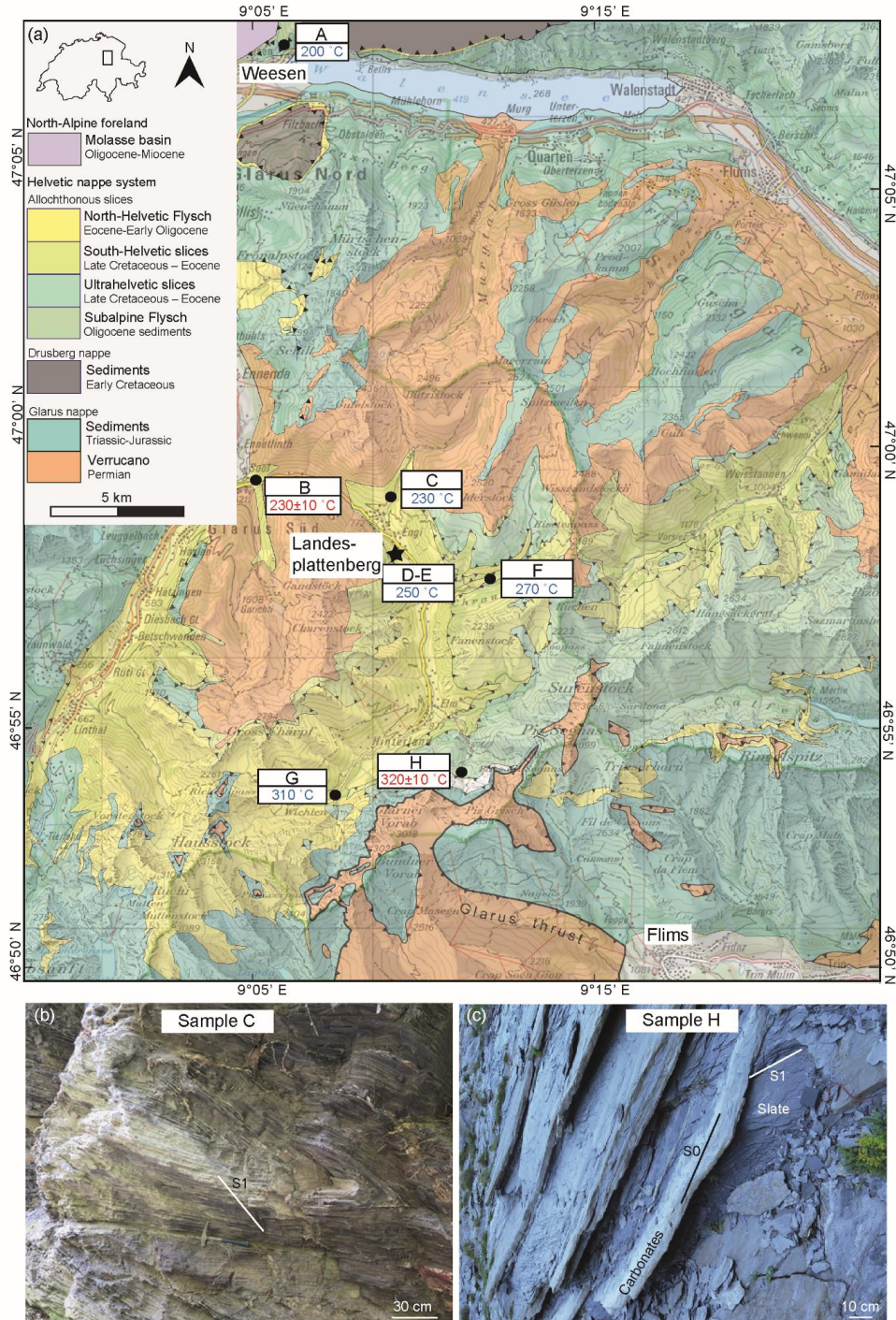
Figure 1. Geological map and outcrops. a) geological map with sample locations. Map adapted from Dielforder et al. (2016), temperatures taken from samples in close vicinity from Ebert et al. (2007) (in red) and from Lahfid et al. (2010) (in blue). Star indicates location of sub-surface samples. b) Outcrop of folded slates at Engi with secondary foliation (46°59'13.9'' N 9°09'17.6'' E) c) Outcrop of slates at Martinsmad (46°53'31.2'' N 9°11'15.5'' E) intercalated with massive carbonaceous layers. S0: bedding, S1:foliation.
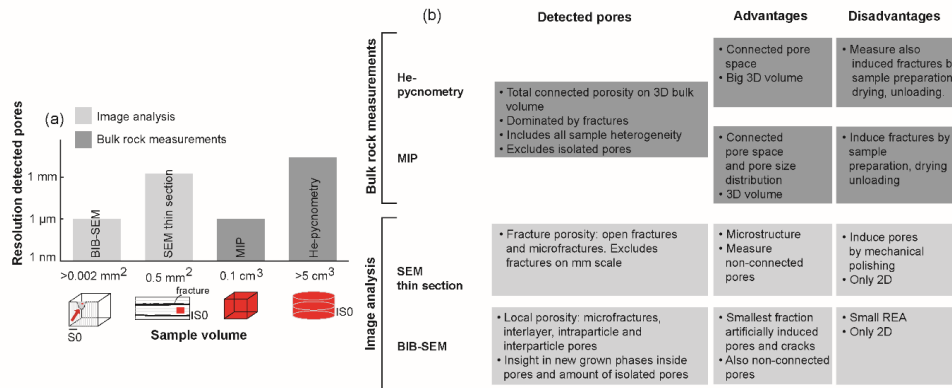
Figure 2. Overview of analytical techniques. a) Sample volume vs. resolution of detected pores. b) Different techniques with advantages and disadvantages. S0: bedding.
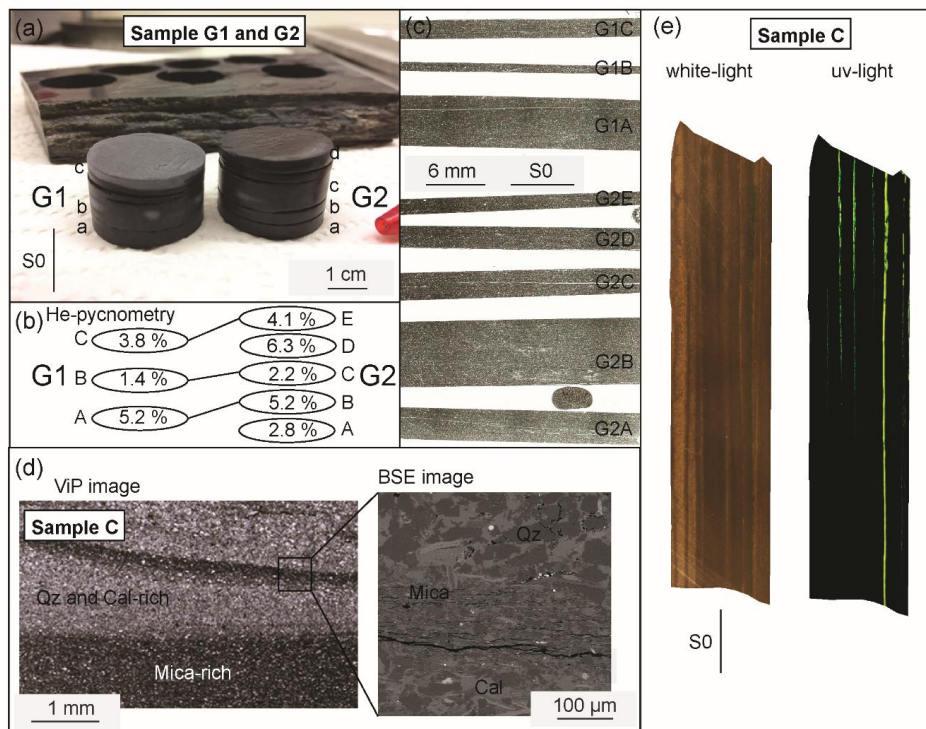
Figure 3. Sample preparation and heterogeneity. a) Sample plugs (G1 and G2) are drilled bedding perpendicular and directly next to each other. The plugs fall apart in sub-samples along the bedding planes. b) Results of He-pycnometry measurements on individual sub-samples from A indicate limited horizontal but substantial vertical variations in porosity. c) Photograph of thin section obtained from sub-sample plugs indicated in A show that the bulk sample is relatively homogeneous. d) Selecting areas of interest from ViP images for further SEM investigation. e) Polished sample C in white and UV-light, note fractures on macroscale. Qz: quartz, Cal: calcite, S0: bedding.
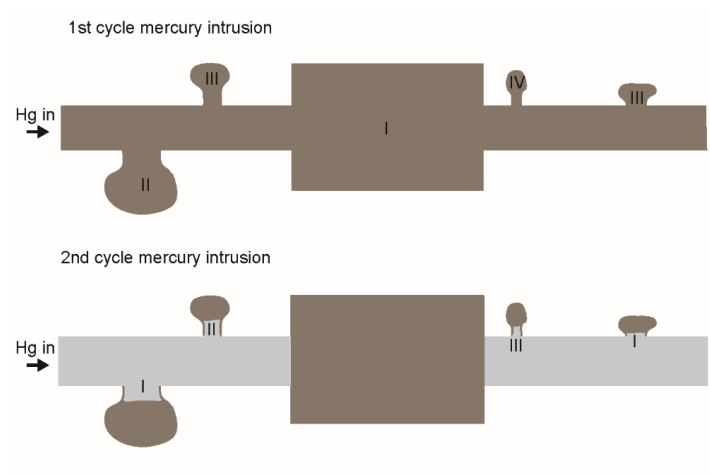
Figure 4. Conceptual model of 1st and 2nd MIP cycle. Numbers indicate the succession in pore filling, which is related to a stepwise increase in pressure, linked to a certain radius of a pore neck entrance. The second cycle indicates the remaining mercury from the first cycle.
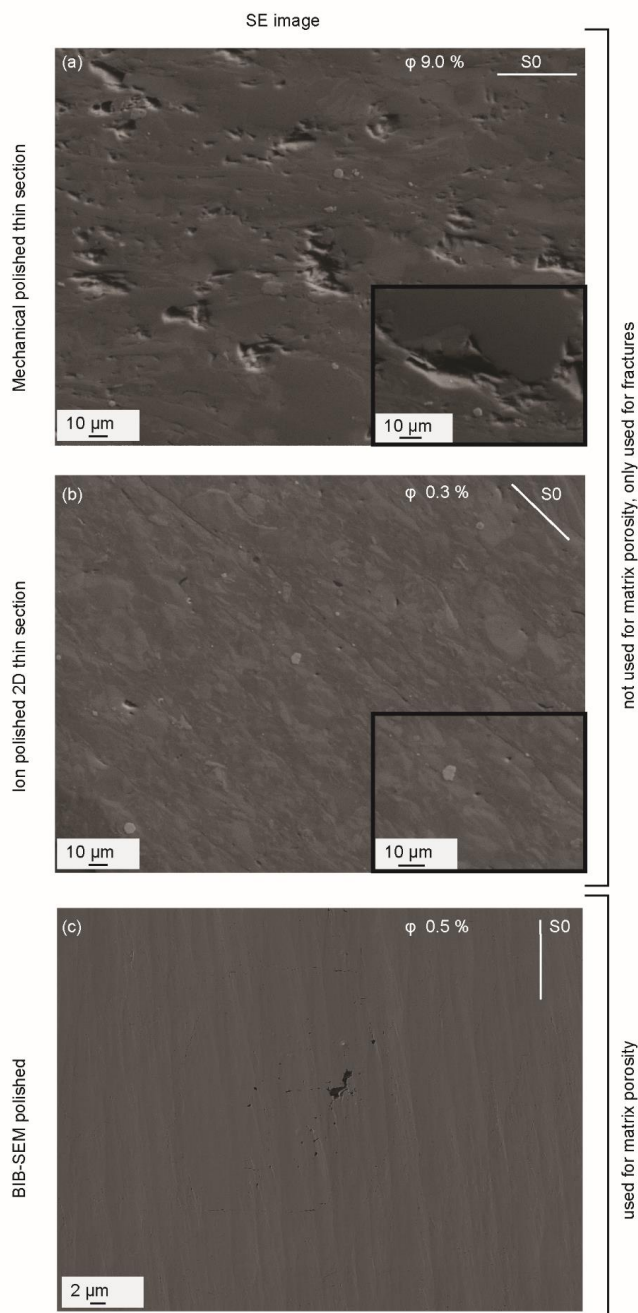
Figure 5. Differences in apparent porosity owing to applied sample polishing techniques in different samples a) Effect of conventional mechanical polishing of thin sections results in an overestimation of porosity owing to severe plugging of grains. b) Ion polished 2D surface of sample taken at 46°53'17.2''N 9°07'40.1''E shows a significantly smaller pore volume compared to the mechanical polishing technique. c) Smoothest surfaces with least induced pores created with BIB-SEM polishing. S0: bedding.
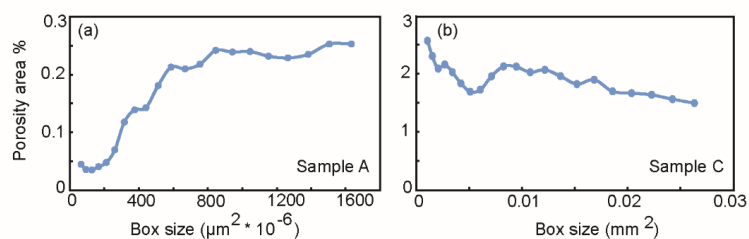
Figure 6. Results of box counting method for BIB-SEM sample A and C. a) Representative Element Area (REA) for sample A is min. 900 µm². b) REA for sample C is min. 25000 µm².
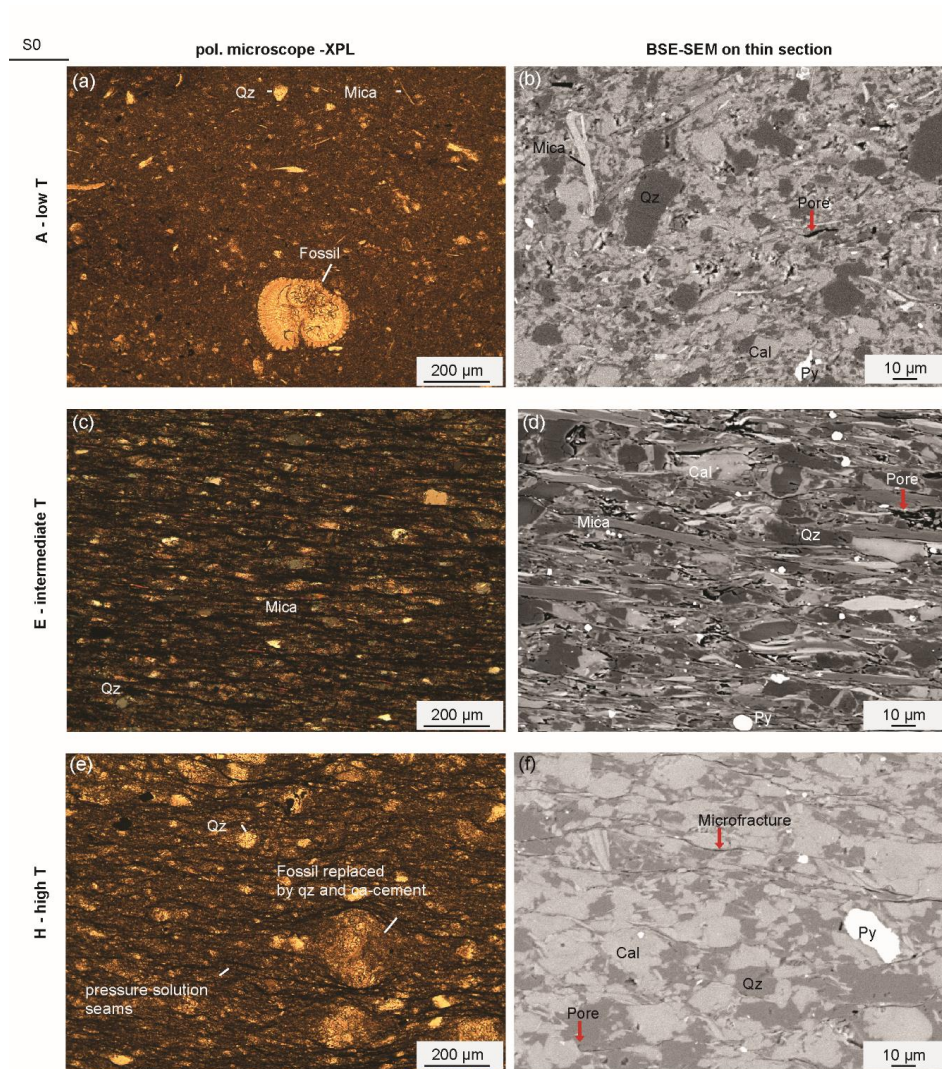
Figure 7. Thin section (left column) and backscatter electron images (right column) of slate microstructures collected along the N-S metamorphic gradient. a-b) sample A: low temperature-low strain end-member – undeformed recrystallized fossils in a former mud matrix with randomly oriented sheet-silicates. c-d) sample E: intermediate temperature-intermediate strain – sheet-silicates aligned bedding parallel. e-f) sample H: high temperature-high strain end-member - showing deformed slate with recrystallized fossils and quartz in a matrix with pressure solution seams parallel to bedding. Qz: quartz, Py: pyrite, Cal: calcite, S0: bedding.
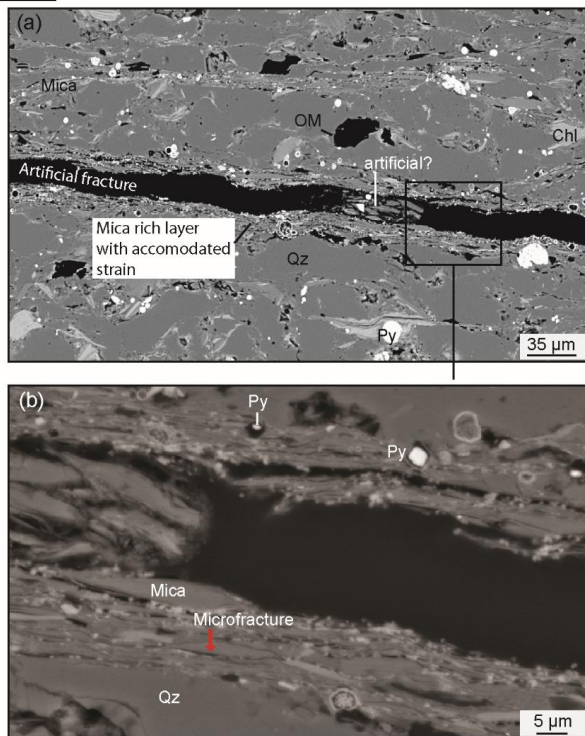
Figure 8. Fracture porosity. a) Coarse-grained quartz-rich layers intercalated with fine-grained sheet-silicate-rich layers in sample F. b) Strain accommodated in fine-grained sheet-silicate-rich layers by alignment of sheet-silicates and the formation of microfractures. OM: organic material, Qz: quartz, Py: pyrite, Chl: chlorite, S0: bedding.
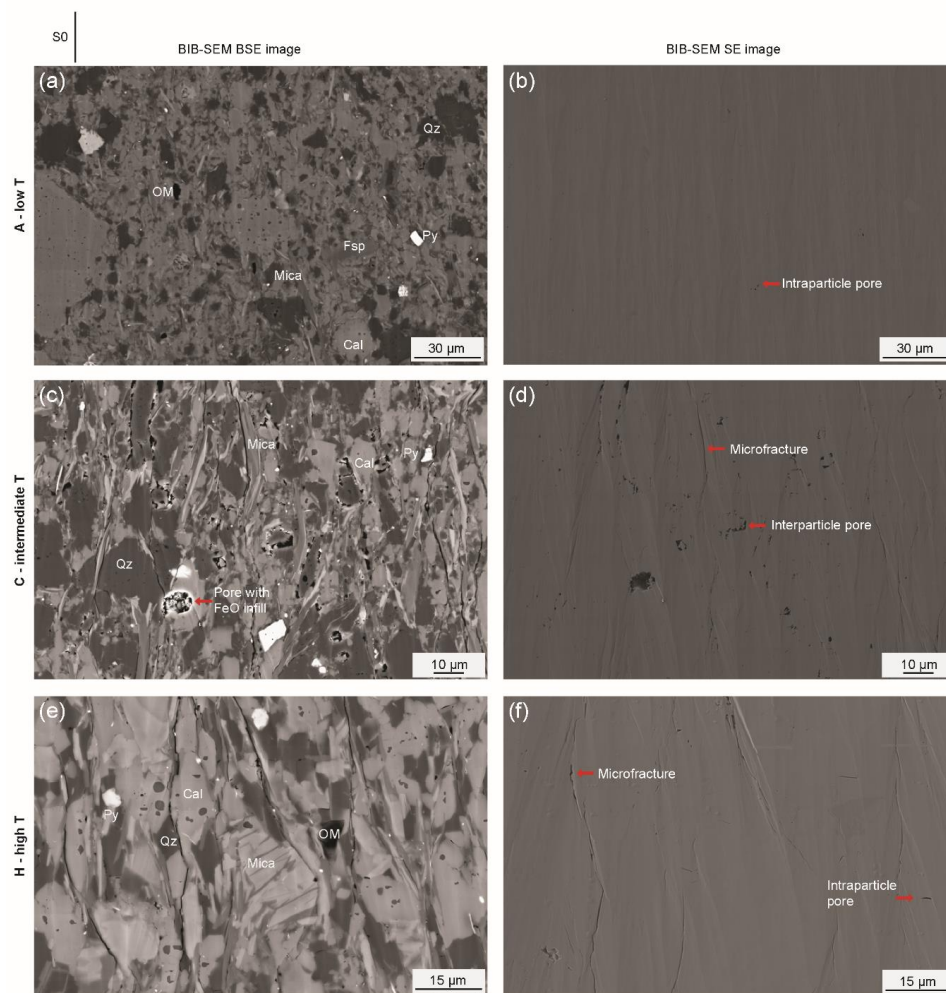
Figure 9. Microstructure and microstructural porosity imaged with BIB-SEM along the temperature gradient. a-b) Low temperature sample A shows smallest porosity, mainly present as intraparticle pores in quartz and dolomite. c-d) Intermediate temperature sample C shows microcracks along sheet-silicates and interparticle pores as effect of dissolution. e-f) High temperature sample H with a defined spaced cleavage shows more microcracks than the intermediate sample C. OM: organic matter, Qz: quartz, Py: pyrite, Fsp: feldspar, Cal: calcite, S0: bedding.
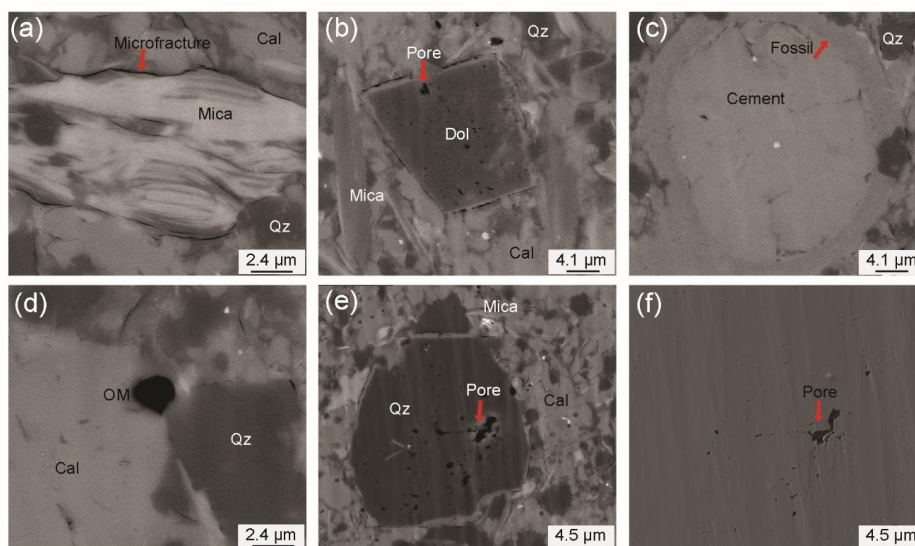
Figure 10. Images of BIB-SEM prepared sub-samples to show different pore morphologies: a) Microfractures occur along grain boundaries of mica aggregates. b) Dissolution pores around and in dolomite (dol) grain. c) Porosity reduction by cement infill of fossils. d) Solid state organic matter (OM), not to be confused with pore-space. e) Intraparticle pores in quartz probably reflecting fluid inclusions. f) SE image of quartz grain with pores in G. Qz: quartz, Cal: calcite.
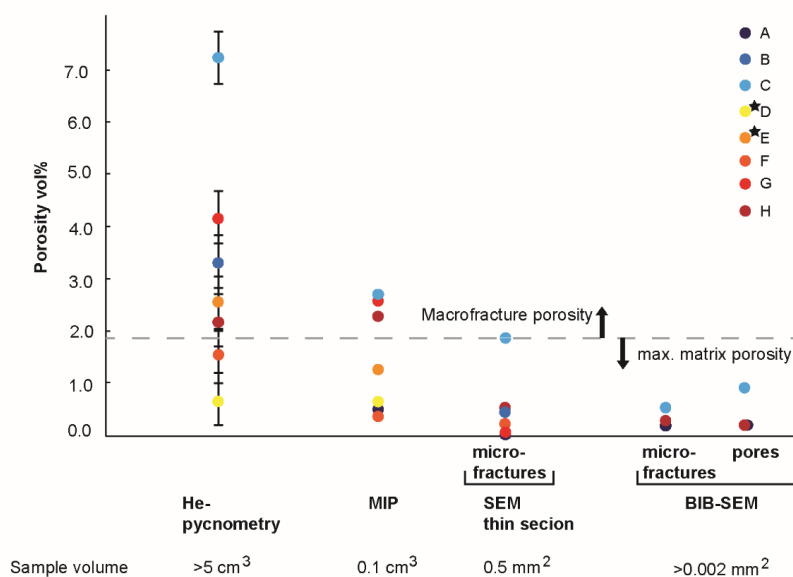
Figure 11. Porosity measurements obtained by five different methods with indicated sample volumes. Stars indicate sub-surface samples. Errors of MIP data and image analysis fall within the data markers itself. Dashed line is threshold between macrofracture porosity (above) and matrix porosity (below).
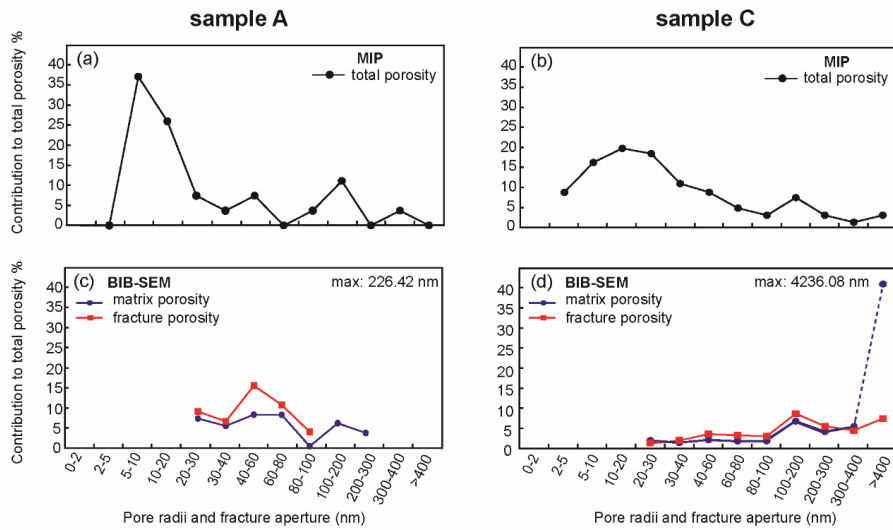
Figure 12. Pore size distributions from MIP compared to image analysis of BIB-SEM images. The pore radius is calculated from the pore area and for the fracture aperture, the minor axis of the calculated fit ellipse is used. a-b) Pore size distributions of MIP results of sample A and C. c-d) Pore size distributions of BIB-SEM analysed sub-samples divided in matrix and fracture porosity. MIP and BIB-SEM distributions show same general trend with peak at the 100–200 nm pore radii. Dashed line: large pore sizes (>300 nm) disturb distributions because of heterogeneity effect.
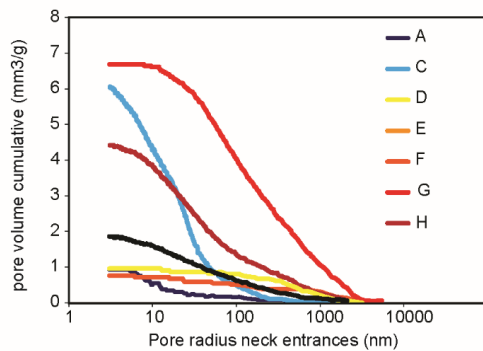
Figure 13. Results from multicycle MIP experiments. Pore radius of the neck entrances vs. cumulative pore volume.
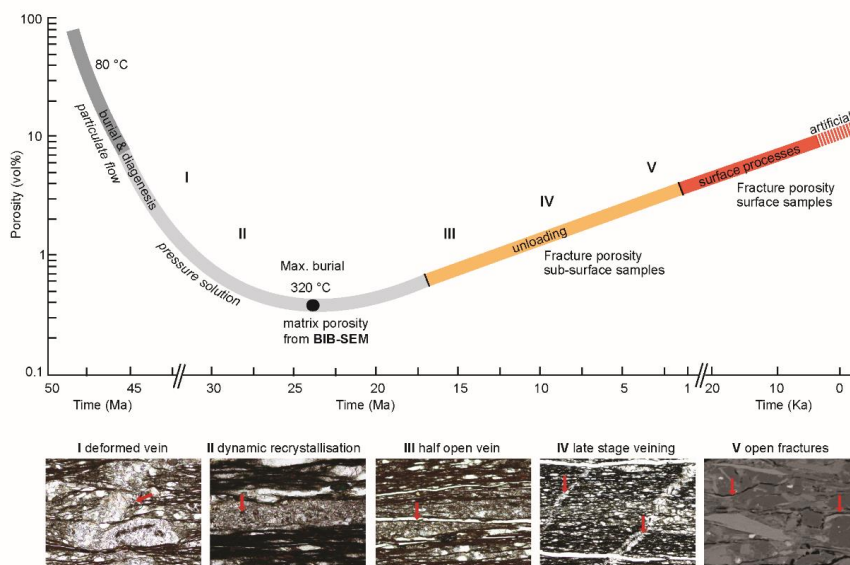
Figure 14. Conceptual porosity evolution over time linked to different vein generations and fractures. Porosity at max. burial is from BIB-SEM, porosity on retrograde path is based on He-pycnometry and MIP data. Boundaries between different domains are estimates. Tectonic processes on prograde path from Dielforder et al. (2015).